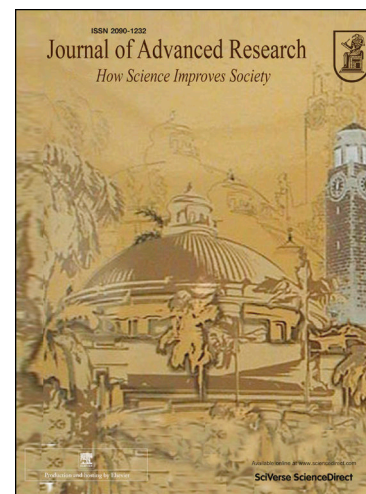


# Journal Pre-proofs



## Original Article

Structural dynamics for highly selective RET kinase inhibition reveal cryptic druggability

Moustafa A. Shehata, Julia Contreras, Ana Martín-Hurtado, Aurane Froux, Hossam T. Mohamed, Ahmed A. El-Sherif, Iván Plaza-Menacho

PII: S2090-1232(22)00116-3  
DOI: <https://doi.org/10.1016/j.jare.2022.05.004>  
Reference: JARE 1195

To appear in: *Journal of Advanced Research*

Received Date: 23 August 2021  
Revised Date: 5 April 2022  
Accepted Date: 5 May 2022

Please cite this article as: Shehata, M.A., Contreras, J., Martín-Hurtado, A., Froux, A., Mohamed, H.T., El-Sherif, A.A., Plaza-Menacho, I., Structural dynamics for highly selective RET kinase inhibition reveal cryptic druggability, *Journal of Advanced Research* (2022), doi: <https://doi.org/10.1016/j.jare.2022.05.004>

This is a PDF file of an article that has undergone enhancements after acceptance, such as the addition of a cover page and metadata, and formatting for readability, but it is not yet the definitive version of record. This version will undergo additional copyediting, typesetting and review before it is published in its final form, but we are providing this version to give early visibility of the article. Please note that, during the production process, errors may be discovered which could affect the content, and all legal disclaimers that apply to the journal pertain.

© 2022 The Authors. Published by Elsevier B.V. on behalf of Cairo University.

1 **Structural dynamics for highly selective RET kinase inhibition**  
2 **reveal cryptic druggability**

3

4 Moustafa A. Shehata <sup>a, b</sup>, Julia Contreras <sup>a</sup>, Ana Martín-Hurtado <sup>a</sup>, Aurane Froux <sup>a</sup>,

5 Hossam T. Mohamed <sup>c, d</sup>, Ahmed A. El-Sherif <sup>b</sup> and Iván Plaza-Menacho <sup>a§</sup>

6 <sup>a</sup> Protein Phosphorylation and Cancer Group

7 Structural Biology, Spanish National Cancer Research Center (CNIO)

8 C/Melchor Fernández Almagro num. 3, 28029 Madrid, Spain

9 Tel.: +34 +34 91 732 8000 (ext. 3030)

10 <sup>b</sup> Chemistry and <sup>c</sup> Zoology Departments, Faculty of Science, Cairo University, Giza

11 12613, Egypt

12 <sup>d</sup> Faculty of Biotechnology, October University for Modern Sciences and Arts, Giza

13 12451, Egypt

14 <sup>§</sup> corresponding author: [iplaza@cnio.es](mailto:iplaza@cnio.es)

15

16

17 **Credit author statement**

18 Conception of the study and experimental design (IP-M), manuscript writing and figure

19 preparation (IP-M and MAS), experimental and biocomputational work (MAS, JC, AM-H,

20 AF and IPM), data processing and analysis (MAS and IPM), academic mentoring to MAS

21 (HTM, AAE)

22

23

24

25

26

27

28 **Structural dynamics for highly selective RET kinase inhibition**  
29 **reveal cryptic druggability**

30  
31 **ABSTRACT**

32 Introduction: The structural and dynamic determinants for highly selective RET kinase  
33 inhibition are poorly understood. Methods-objective: Here we demonstrate by applying  
34 an integrated structural, computational and biochemical approach that the druggability  
35 landscape of the RET active site is determined by the conformational setting of the ATP-  
36 binding (P-) loop and its coordination with the  $\alpha$ C helix. Results: Open and intermediate  
37 P-loop structures display additional druggable vulnerabilities within the active site that  
38 were not exploited by first generation RET inhibitors. We identify a cryptic pocket  
39 adjacent to the catalytic lysine formed by K758, L760, E768 and L772, that we name the  
40 post-lysine pocket, with higher druggability potential than the adenine-binding site and  
41 with important implications in the regulation of phospho-tyrosine kinase activity. Crystal  
42 structure and simulation data show that the binding mode of highly-selective RET kinase  
43 inhibitors LOXO-292 and BLU-667 is controlled by a synchronous open P-loop and  $\alpha$ C-  
44 in configuration that allows accessibility to the post-lysine pocket. Molecular dynamics  
45 simulation show that these inhibitors efficiently occupy the post-lysine pocket with high  
46 stability through the simulation time-scale (300 ns), with both inhibitors forming  
47 hydrophobic contacts in the pocket further stabilized by pi-cation interactions with the  
48 catalytic K758. Engineered mutants targeting the post-lysine pocket impact on inhibitor  
49 binding and sensitivity, as well as RET tyrosine kinase activity. Conclusions: The  
50 identification of the post-lysine pocket as a cryptic druggable vulnerability in the RET  
51 kinase and its exploitation by second generation RET inhibitors has important  
52 implications for future drug design and the development of personalized therapies for  
53 patients with RET-driven cancers

54

55 **Key words**

56 Protein kinases, oncogene, structure-function, targeted-therapies, drug-discovery

57 **INTRODUCTION**

58 Protein kinases play a causative role in human disease and cancer when deregulated  
59 by oncogenic mutations or overexpression (1). A current hallmark for precision and  
60 personalized medicine is the development of highly specific protein kinase inhibitors that  
61 can be translated into the clinic for the successful treatment of cancer patients (2). To  
62 date, the U.S. Food and Drug Administration (FDA) has approved more than 30 kinase  
63 inhibitors that are used in the clinic to treat cancer and other human disorders (3).  
64 However, these drugs target only a small percentage of the entire human kinome (5%)  
65 and they usually display non-specific crosstalk and lack of activity against drug-resistant  
66 secondary mutations (3).

67 The *RET* (REarranged-during Transfection) proto-oncogene encodes a receptor tyrosine  
68 kinase for members of the glial cell line-derived neurotrophic factor (GDNF) family of  
69 extracellular ligands (4). Oncogenic *RET* mutations and rearrangements results in  
70 constitutive ligand-independent activation of RET catalytic activity and signalling (4).  
71 Both fusions and mutated RET are actionable drivers in non-small cell lung cancer  
72 (NSCLC) and thyroid cancers (5,6). In particular, *RET* rearrangements have been  
73 identified in ~2% of lung adenocarcinomas (NSCLC), 20% of papillary thyroid carcinoma  
74 (PTC), and less frequently in other types of cancer including breast, salivary gland  
75 intraductal carcinoma, pancreatic and colon cancers (5-9).

76 Rational and precise targeting of oncogenic drivers is a crucial hallmark in the cancer  
77 research field. Over the last years, the FDA approved the repurposing of several multi-  
78 tyrosine kinase inhibitors (MKIs) with pharmacological activity against RET for the  
79 treatment of thyroid, lung adenocarcinoma and other RET-positive cancers (10). These  
80 inhibitors tested in the clinic had significant limitations due to non-selective activity  
81 against multiple kinases, dose-limiting toxicities as well as suboptimal target inhibition in  
82 the presence of resistance-associated secondary mutations, resulting altogether in  
83 modest survival outcomes in a limited subset of patients compared with other targeted  
84 therapies clinically successful. Overall, the clinical outcomes in response to RET-

85 directed therapies were limited and modest compared with those achieved with other  
86 drugs targeting other oncogenes in solid tumors including EGFR, B-RAF, ALK, and  
87 ROS1 (11,12).

88 Recently developed RET inhibitors LOXO-292 (selpercatinib) and BLU-667 (pralsetinib)  
89 exhibited >100-fold selectivity against a wide variety of RET oncogenic mutations in  
90 preclinical and clinical models (13-15). Data from the phase I clinical trial (ARROW)  
91 revealed that BLU-667 treatment resulted in a substantial response in RET-rearranged  
92 NSCLC patients with overall response rate (ORR) of 60% and disease control rate (DCR)  
93 of 100% (14). Additionally, clinical global phase I/II trial of LOXO-292 (LIBRETTO-001)  
94 for RET rearranged-positive NSCLC showed substantial response as a potent inhibitor  
95 with ORR of 68%, median progression-free survival (PFS) of 18.5 months, and median  
96 duration of response of 20.3 months (13,15). LOXO-292 also demonstrated a high ORR  
97 of 91% in NSCLC patients with central nervous system metastasis (16,17). In the  
98 registration dataset of RET-mutant MTC, the acquired clinical trial data showed ORR of  
99 56% and 53%, in multi-kinase inhibitors (MKI)-treated and MKI-naive patients,  
100 respectively. Another clinical study including 26 patients with RET-fusion positive PTC  
101 showed 62% ORR (18). As a consequence, the FDA recently approved LOXO-292 and  
102 BLU-667 for the treatment of cancer patients presenting oncogenic *RET* rearrangements  
103 or mutations (16,19). Despite such promising scenario, recurrent mechanisms of  
104 resistance to these selective inhibitors have already been described (20-22). In  
105 particular, refractory mutations located at the solvent front pocket (21). Understanding  
106 these mechanisms of resistance as well as the structural dynamics and pharmacophoric  
107 features required for highly specific and effective RET kinase inhibition is a crucial step  
108 for the design and development of clinically successful compounds able to overcome  
109 refractory RET mutations. In this study we apply an integrated approach combining  
110 structural, molecular dynamic simulations, together with functional analyses in order to  
111 define the druggability landscape of the RET active site and the molecular mechanism  
112 behind highly selective second generation RET inhibitors LOXO-292 and BLU-667.

## 113 MATERIAL AND METHODS

### 114 Mapping of ligand binding site and hotspot residues

115 FTSite server (23) was used to explore the druggable pockets within the active site of  
116 RET in crystal structures with different P-loop conformations including closed- (PDB  
117 2IVS), intermediate- (PDB 2IVT), and open- conformers (PDB 5AMN).

118

### 119 Transient pocket analyses

120 Mapping of transient pockets within the RET active site was performed by the TRAnsient  
121 Pockets in Protein (TRAPP) pipeline (24,25). The overall workflow of the TRAPP  
122 webserver consists of three stages: i) ensemble of the generated structures, ii)  
123 superimposition and clustering and iii) detection and characterization. The TRAPP  
124 structure module contains several simulation methods for the generation of protein  
125 ensembles. The pseudo-ligand (RIPlig) and Langevin rotamerically induced  
126 perturbations (L-RIP) MD-based methods were used for the generation of protein  
127 ensembles. Following each perturbation, the structures were relaxed for 0.6 ps in an  
128 implicit solvent MD simulation coupled to a Langevin thermostat. The TRAPP analysis  
129 module was used to align and superimpose the generated structures using the backbone  
130 of the previously chosen binding pocket residues using the RMSD metric, and clustered  
131 using a hierarchal algorithm with an RMSD threshold value of 3 Å. The TRAPP pocket  
132 module was employed to identify transient regions within the active site. The protein  
133 cavities near the binding pocket are calculated and saved on the grid. Furthermore, the  
134 physicochemical properties of the side chain residues in the detected cavities, surface  
135 area, and pocket are computed by this module.

136

### 137 Classical MD simulation

138 MD simulation was performed using the Amber 16 software package with GPU  
139 acceleration (26). In particular, the ff14SB (27) and GAFF (generalized Amber force field)  
140 (28) for proteins and ligands, respectively, and the TIP3P model was chosen for water

141 molecules. The partial charges of each ligand were calculated implemented in the AM1-  
142 BCC charge method using the Antechamber module from AmberTools 16. Proteins were  
143 protonated at pH 7.4 and each molecular ensemble was immersed in a cubic box with  
144 a separation margin from the surface of the solute of 10 Å. The system was  
145 electroneutralized by addition of sufficient Cl<sup>-</sup> counterions. The long-range electrostatic  
146 interactions were treated by the Particle Mesh Ewald (PME) method (29), while the short-  
147 range interactions; electrostatic and van der Waal, were calculated with a distance cut-  
148 off of 8 Å. The SHAKE algorithm (30) was applied to constrain the bond lengths involving  
149 hydrogen atoms to their equal volumes. The integration time step was 2fs. The systems  
150 were energy minimized in two stages (a total of 5000 steps): I) Minimization of water  
151 molecules around the solute was run for 5000 steps, with 4000 steps of steepest descent  
152 and then 1000 steps of a conjugate gradient algorithm with a restraint force of 10  
153 Kcal/molÅ<sup>2</sup> applied to restrain the solute atoms; II) Minimization of the entire system was  
154 run for the same number of steps as the previous stage, but with no restraint force  
155 applied. Following that, each system was heated to 300°C in an NVT ensemble for 150  
156 ps with a positional restraint of 10 Kcal/molÅ<sup>2</sup> applied to protein atoms. The system  
157 pressure was then held constant at 1 atm for 1 nanosecond under NPT ensemble.  
158 Finally, the production phase was carried out for 300 nanoseconds under NPT ensemble  
159 at 300K and 1 atm with no positional constraints. The system coordinates were saved  
160 every 10 ps. The generated trajectories were analyzed using CPPTRAJ from the  
161 AmberTools 17. Finally, hydrogen bond analysis was carried out by VMD hydrogen  
162 bonds tools with distance and angle cut-offs of 3.0 Å and 135 degrees, respectively. All  
163 the plots were generated by Gnuplot and Python matplotlib (31).

164

### 165 **Binding free energy calculations using MM-GBSA method**

166 The Molecular Mechanics Generalized Boltzmann Surface Area (MM-GBSA) method  
167 was employed for binding free energy calculations using an implicit solvent model. This

168 method additionally allows the energy decomposition analysis, which provides detailed  
 169 information about the residual energetic contributions (32,33). The free energy of ligand  
 170 binding to the receptor to form a complex is estimated using the following equations:

$$171 \quad \Delta G_{\text{(bind)}} = G_{\text{(RL)}} - G_{\text{(R)}} - G_{\text{(L)}}$$

172 It is further decomposed into several contributed interactions:

$$173 \quad \Delta G_{\text{(bind)}} = \Delta H - T\Delta S = \Delta E_{\text{(MM)}} + \Delta G_{\text{(sol)}} - T\Delta S$$

174 In which:

$$175 \quad \Delta E_{\text{(MM)}} = \Delta E_{\text{(int)}} + \Delta E_{\text{(ele)}} + \Delta E_{\text{(vdw)}}$$

$$176 \quad \Delta G_{\text{(sol)}} = \Delta G_{\text{(PB/GB)}} + \Delta G_{\text{(SA)}}$$

$$177 \quad \Delta G_{\text{(SA)}} = \gamma \cdot \text{SASA} + b$$

178

179  $\Delta G_{\text{bind}}$  is the interaction energy between the receptor and ligand in a vacuum,  
 180 equivalent to the sum of polar ( $\Delta G_{\text{PB/GB}}$ ) and non-polar ( $\Delta G_{\text{SA}}$ ) interactions between  
 181 the solute and the continuum solvent model. The GB model used for the calculation of  
 182 polar interactions provides an analytical expression of the polar interactions, which is  
 183 faster than the Poisson Boltzman (PB) method. The Generalized Boltzman (GB) model  
 184 (ig=2) was used to measure the electrostatic solvation energy (34). The per residue  
 185 energy decomposition method implemented in the MM/GBSA was used to analyze the  
 186 residual energy interaction contribution to the total binding free energy. This method  
 187 considers the intermolecular and solvation energies without the inclusion of the entropy  
 188 (35).

189

### 190 **Site directed mutagenesis**

191 Site directed mutagenesis was performed on: i) a pBac-PAK-RET construct codifying  
 192 codon optimized kinase domain (KD, aa 705-1013) and ii) pRC-CMV-RET isoform 9 (aa,  
 193 1-1072) as templates using a modified Q5-polymerase-based protocol in which  
 194 complementary primers were employed followed by DpnI treatment at 37 °C for at least  
 195 120 min before transformation in Q5-DH5 $\alpha$  bacterial strain. Mutagenesis was validated  
 196 by Sanger sequencing.

197



**198 Expression and purification of recombinant RET KD**

199 Expression of (codon optimized) RET KD (WT and indicated mutants) was performed in  
200 Sf9 insect cells using a baculovirus system following already established and published  
201 protocols (36). Protein purification was performed by tandem IMAC ( $\text{Ni}^{+2}$ ) and  
202 Glutathione-beads gravity flow chromatography and in-gel 3C-protease digestion (36-  
203 38).

204

**205 Differential Scanning Fluorimetry (DSF)**

206 To evaluate the thermal stability of RET kinase WT and indicated mutants in the absence  
207 of (apo) and in complex with inhibitors LOXO-292, BLU-667 and ZD6474 (vandetanib)  
208 as control, we applied two different DSF methods. First, an indirect SYPRO Orange-  
209 based method. For this assay the total reaction volume was adjusted to 40  $\mu\text{L}$  at 1-2  $\mu\text{M}$   
210 protein, 10  $\mu\text{M}$  inhibitor, and 2xSYPRO Orange concentrations subjected to a gradient  
211 of temperature from 20 to 95  $^{\circ}\text{C}$ . Fluorescence was measured on an Applied Biosystem  
212 7300 Real-Time PCR system. Second, a direct method based on changes in intrinsic  
213 fluorescence upon a quick gradient of temperature was measured using a tycho  
214 nanotemper instrument following manufacturer's instructions.

215

**216 Western-blotting**

217 Western blotting (WBs) experiments were performed as previously described (38,39).  
218 For auto-phosphorylation assays with recombinant proteins, 2.5-5  $\mu\text{M}$  of isolated RET  
219 KD (WT and indicated mutants) was incubated with 2 mM  $\text{MgCl}_2$  and 1 mM ATP for the  
220 indicated time points, after which samples were mixed with 5X sample loading buffer and  
221 boiled for 5 min. For cell lysates, transfected HEK293 cells subjected to the indicated  
222 concentrations of drug treatment were lysed in ice-cold 20 mM Tris pH 7.5, 150 mM  
223 NaCl, 2 mM DTT, 2.5% glycerol, supplemented with a cocktail of protease and  
224 phosphatase inhibitors and the total cell extract was centrifuged for 15 min at 5000-6000  
225 rpm, after which soluble sample was mixed with 5x sample buffer and boiled for 5 min

226 prior protein quantification with Bradford. Equal amounts of samples were run in SDS-  
227 PAGE gels and subjected to immunoblotting using the indicated antibodies.

## 228 RESULTS

### 229 1. RET druggability is determined by the dynamics of the P-loop

230 We explored the druggability landscape of the RET active site (Fig. S1) under different  
231 P-loop configurations. Our rationale was driven by a previously solved high-resolution  
232 crystal structure of a RET KD displaying two discrete conformations of the P- loop (36).  
233 In the closed structure the F735 (P-loop) side chain is clamped over the active site and  
234 the side chain of  $\alpha$ C E768 points away from the cleft. This conformer was further  
235 stabilized by a triad of tethered residues between E734 (P-loop), R912 (activation loop,  
236 A-loop) and D771 ( $\alpha$ C) (Fig. 1A). In contrast, in the open structure, the F735 side chain  
237 was solvent-exposed through a large displacement of the loop from the active site,  
238 whereas E768 points inward into the cleft. The two different conformations are defined  
239 by the mutually exclusive configurations of E768 and F735 side chains, which restrict  
240 nucleotide binding and accessibility. The open structure is further stabilized by salt-  
241 bridge and hydrogen bonding interactions between residues from the P- and the  $\beta$ 3- $\alpha$ C  
242 loops (Fig. 1A). First, we measured the conformational space within the active site of  
243 RET using several crystal structures capturing different P-loop conformational states:  
244 2IVS (closed), 2IVT (intermediate), 5AMN (open) and 4CKJ (open and closed), by  
245 calculating the center of mass distance between the  $\beta$ 3 catalytic K758 side chain (NZ  
246 atom) and P-loop E734 main chain ( $C\alpha$ ) and their corresponding active site volumes  
247 (figure 1B, and table S1). While distances (and volumes) in the closed and intermediate  
248 states were 7.6 Å (646.623 Å<sup>3</sup>) and 8.5 Å (902.283 Å<sup>3</sup>), respectively, the open state  
249 showed significant larger values of 15.0 and 16.6 Å (1870.6 and 2311.7 Å<sup>3</sup>). Transition  
250 from a closed to an open P-loop state was also associated with an increase in the  
251 distance between the gatekeeper residue V804 and the catalytic K758 (table S1). These  
252 data indicated to us that a larger druggability space within the active site of RET is

253 available in the opened structure. Next, we mapped druggable regions within the active  
254 site of RET susceptible to conformational changes by the P-loop using the FTSite (Fig.  
255 1C-E and table S2).

256 Three pockets were identified and ranked within the active site of RET in the open  
257 structure (Fig. 1C). The adenine-binding pocket (ABP) linked to the front pocket-I (FP-I),  
258 and gatekeeper pocket (in green) displayed average druggable scores. A small pocket  
259 adjacent to the catalytic loop-HRD motif pocket (CP, purple) made up of D874, R878,  
260 N879 and P914 side chains together with R912 main chain was detected with low  
261 druggability score (see table S2 for details). Interestingly, a small pocket with maximum  
262 druggability potential was detected in the front-pocket-II adjacent to the catalytic lysine  
263 (in pink) defined by K758 ( $\beta$ 3), L760 ( $\beta$ 3- $\alpha$ C loop), E768 ( $\alpha$ C), and L772 ( $\alpha$ C). In the  
264 case of the intermediate structure (Fig. 1D, right panel) the ABP and FP-I (pink) ranked  
265 as the top druggable pocket. The CP (purple) was also detected with averaged druggable  
266 potential. We noticed that the FP-II was not detected as it was partially occupied by the  
267 P-loop, in particular F735 side chain (Fig. 1D, right panel). This is in contrast with another  
268 intermediate RET crystal structure in which F735 side chain electron density is not  
269 defined (PDB 2IVV). In this situation the FP-II is partially accessible and appears as the  
270 top ranked druggable region (Fig. 1D, right and central panels). In the case of the closed  
271 structure (Fig. 1F) only the ABP and FP-I region appear as druggable. This is attributed  
272 to the degree of occupancy of the active site by F735 side chain and the P-loop itself  
273 impeding the access to the front solvent pocket-II. These data highlight: i) the existence  
274 of additional druggable vulnerabilities within the active site that were not exploited by first  
275 generation RET inhibitors, and ii) that optimal and selective RET kinase inhibition will  
276 depend on interactions other than those taking place at the adenine-binding and  
277 gatekeeper pockets.

278 **2. Extensive perturbation of the active site disrupts the closed tether by inducing**  
279 **an open-P-loop**

280 To simulate the perturbation of the active site of RET by an inhibitor able to exploit an  
281 extensive druggable space and its impact on the transition from a closed to an open  
282 GRP-loop, we applied RIP (rotamerically induced perturbations) MD simulations  
283 methods. The RIP-MD method is a recent MD simulation technique that allows the  
284 generation of local perturbations in proteins that are capable of inducing large  
285 conformational changes of several Å in just picoseconds of a MD simulation (24). It is  
286 particularly useful for identifying potentially mobile loops and helices in a protein  
287 structure, with important implications also y drug binding and catalytic inhibition. First,  
288 we used the RIPlig (RIP by a pseudo-ligand) method to identify large conformational  
289 changes within the active site. In the case of RET, this approach resulted in a significant  
290 10 Å displacement of the P-loop from a closed tether to a fully open solvent accessible  
291 configuration as indicated by a large displacement of E734 (Fig. S2A). These data were  
292 in good agreement with the crystal structure data (36) and the rationale of our study (see  
293 figure 1). Next, we applied the Langevin-RIP (L-RIP) approach by perturbing the dihedral  
294 angles of residues E734 and F735, both key determinants from our MD and X-ray data,  
295 to evaluate their specific contribution in P-loop transition (Fig. S2B). Perturbation of the  
296 dihedral angles of these two residues resulted in intermediate P-loop configurations  
297 associated with significant changes in the druggability potential and modification of active  
298 site physicochemical properties. Whereas perturbation of E734 resulted in lower and less  
299 consistent conformational changes in the P-loop and druggability, as indicated by volume  
300 and exposure values. Other physicochemical properties e.g. hydrophobicity, hydrogen  
301 acceptor, and negative ion dependencies were increased in some particular frames. On  
302 the other hand, F735 perturbation resulted in higher druggability potential and the  
303 induction of complex conformational changes, as evidenced by higher volume and  
304 exposure values, which in turn resulted in increased hydrophobicity, hydrogen acceptor,  
305 and negative charges of the active site (Fig. S2B). Furthermore, we found that residues  
306 from the P-loop (aa 730-739),  $\alpha$ C helix (aa 766-773),  $\beta$ 3-  $\alpha$ C loop (aa 756-760) and hinge  
307 (aa 805-810) regions showed highly dynamic behavior (Fig. S2C) indicative of significant

308 motions by the P-loop and its coordination with other secondary structural elements such  
309 the  $\alpha$ C helix,  $\beta$ 3-  $\alpha$ C loop and hinge. Furthermore, the two trajectories revealed several  
310 druggable pockets within the active site with high occurrence throughout the simulation  
311 (Fig. S2D) that matched the druggable space observed in the open and intermediate  
312 crystal structures by the FTSite method comprising the solvent front pocket (ABP), front  
313 pocket-I (FP-I) and front pocket-II (FP-II) (Fig. S2E). These results were in good  
314 agreement with the FTSite analyses and showed that perturbation of the closed  
315 autoinhibitory tether causes a large conformational motion of the P-loop expanding the  
316 druggability landscape of the RET kinase active site.

317

### 318 **3. Identification and dynamic characterization of a cryptic and druggable pocket**

319 The FTSite analyses revealed a sub-pocket adjacent to the catalytic lysine consisting of  
320 K758 ( $\beta$ 3), L760 ( $\beta$ 3- $\alpha$ C loop), E768 ( $\alpha$ C), and L772 ( $\alpha$ C) that we name post-lysine  
321 pocket (Fig. 1C). This pocket is defined in a central axis by hydrophobic L760 and L772,  
322 which are flanked on one side by catalytic K758 and E768 on the other (Fig. 1C-D). While  
323 in the closed and intermediate configurations F735 points to the center of the pocket, in  
324 the open structure F735 points away from the cleft and the side chain of E768 adopts  
325 an inner position together with K758, defining a fully accessible post-lysine pocket (Fig.  
326 2A). We consistently observed an invariant  $\alpha$ C helix-in (active) in the different  
327 configurations with a proper alignment of the regulatory and catalytic spine residues in a  
328 DFG-in state (Fig. S3). This newly identify druggable pocket appears to be evolutionary  
329 conserved (Fig. 3B), next we examined the presence and conservation of the FP-II and  
330 post-lysine pocket in other protein kinases that are pharmacologically inhibited by RET  
331 tyrosine kinase inhibitors (40) for which crystal structure data are available (Fig. 2C),  
332 including ALK (PDB 4TT7), VEGFR1 (3HNG), VEGFR2 (3VHE), MET (3DKC), Tie-2  
333 (2OSC), TrKB (4ASZ), Axl (5U6B), ROS1 (3ZBF), FGFR1 (4V05), FGFR2 (1GJO),  
334 FGFR3 (6LVM), FGFR4 (4XCU), c-*Src* (4U5J), PDGFR $\alpha$  (6JOL), Abl (3IK3), EGFR

335 (5Y9T) and B-RAF (3C4C). From this set of structures, we looked at the conservation of  
336 the residues defining the post-lysine pocket. RET F735 (P-loop) and L760 ( $\beta$ 3- $\alpha$ C loop)  
337 were highly conserved residues within the dataset, with exceptions only in c-Abl (Y253)  
338 at the equivalent position to F735 and Tie-2 (M857) and Axl (M569) in the equivalent  
339 position to L760. An acidic residue equivalent to RET E768 ( $\alpha$ C) lacked conservation in  
340 TrKB (A597), c-Src (S303), EGFR (A755) and B-RAF (Q494). RET L772 was substituted  
341 by phenylalanine in the case of ALK, Tie-2, TrKB, Axl, Ros, c-Src, Abl, B-RAF or  
342 isoleucine in the case of EGFR. These data indicate that the conservation of residues  
343 defining the post-lysine pocket occurred within the closest RET phylogenetic group of  
344 receptor tyrosine kinases including FGFR1, FGFR2, FGFR3, FGFR4, VEGFR1,  
345 VEGFR2, and PDGFR $\alpha$  (Fig. 2C and S4). Interestingly, the majority of the indicated  
346 structures have a P-loop-closed and/or an  $\alpha$ C-out configuration relative to RET, which  
347 results in a non-accessible post-lysine pocket (Fig. 2D-E). Using FTSite, a druggable  
348 post-lysine pocket was only detectable in structures with  $\alpha$ C-in and open P-loop  
349 conformers including RET and FGFR2 (PDB 2PVF). In the latter, however, despite  
350 displaying an accessible post-lysine pocket the FP-II did not appear as druggable,  
351 probably as a consequence of the  $\alpha$ C being slightly shifted toward an intermediate  
352 position (Fig. S4A). To further corroborate the dynamic crosstalk between the P-loop and  
353  $\alpha$ C helix to restrict or allow access to the post-lysine pocket, we analyzed the druggable  
354 pockets in the FGFR-3 active site using the FTSite. The catalytic domain of FGFR3 (PDB  
355 6LVM) displayed a very similar conformation to FGFR2 with RMSD value of 0.6 Å, with  
356  $\alpha$ C-in but closed P-loop configuration. As predicted, neither the FP-II nor post-lysine  
357 pocket were identified as druggable sites in the FGFR3 structure (Fig. S4B)

358 These data demonstrated that conservation of the post-lysine pocket is a common  
359 feature of RET closest RTKs phylogenetic group, but this fact is not sufficient for  
360 occupancy as dynamic inputs from P-loop and  $\alpha$ C restrict access to the pocket. A fully  
361 accessible and druggable post-lysine pocket requires of a P-loop-open and  $\alpha$ C-in

362 configuration that are only seen in RET kinase crystal structures, as illustrated in figure  
363 2E.

364

#### 365 **4. LOXO-292 and BLU-667 target the post-lysine pocket**

366 We explored the binding mode of highly specific RET inhibitors LOXO-292 and BLU-667  
367 under different P-loop configurations. The two compounds were able to accommodate  
368 properly into the active site of RET only in an open state (21,22,41). Superimposition  
369 with intermediate (2IVV) or closed (2IVS) RET structures (Fig. 3A and B) demonstrated  
370 that both compounds would clash with the loop in those settings in which compounds  
371 are restricted to accommodate only onto the adenine-binding pocket, as seen in the  
372 crystal structures of RET KD in complex with vandetanib and PP1 (37,38). Opening of  
373 the P-loop results in suitable occupancy of the FP-II and the post-lysine pocket by LOXO-  
374 292 and BLU-667, respectively (Fig. 3A and B). Despite their atypical binding modes,  
375 both inhibitors do bind into a DFG-in (active) configuration with proper alignment of the  
376 regulatory (R-) and catalytic (C-) spines contrary to type II inhibitors, which perturb such  
377 alignment of the spines, see figure S3 (38,42,43).

378 BLU-667 (pralsetinib) targets the post-lysine pocket by accommodating the 4-  
379 fluoropyrazole ring into the patch forming a pi-cation interaction with the catalytic K758  
380 and the fluorine group forming hydrophobic contacts with post-lysine pocket residues  
381 L760 and L772. Three hydrogen bonds were formed with E805 and A807 from the hinge  
382 region by the 5-methyl-pyrazol group with additional hydrophobic interactions with A756,  
383 V804, L881, I788 and V738. The methyl-pyrimidine group forms hydrophobic contacts  
384 with L730 in addition to coordinating with one water molecule via the N1. Of note there  
385 are two other water molecules coordinated with the compound: one with N2 of the 4-  
386 fluoropyrazole group, and the other with the methoxy oxygen bounded to the  
387 cyclohexane ring (Fig. 3C).

388 LOXO-292 (selpercatinib) targeted the post-lysine pocket by accommodating the 2-  
389 methoxypyridine ring and forming also a pi-cation interaction with K758. The



390 pyrazolo[1,5-a] pyridine group forms an additional hydrogen bond with the main chain  
391 nitrogen atom of A807 at the hinge and hydrophobic interactions with L730 and L881.  
392 Further hydrophobic contacts were made by the central pyridine group and V738. Two  
393 water molecules are coordinated with the oxygen atoms from the 2-methoxypyridine  
394 group and the pyrazolo[1,5-a] pyridine ring, respectively.

395 Both compounds appeared to exploit extensive ATP binding mimicry when compared to  
396 first-generation RET inhibitors whose prototypical interactions are mostly limited to the  
397 hinge and adenine-binding site. In fact, both compounds could only accommodate into  
398 the active site in an open state (Fig. 3A-B) as the P-loop would clash with the compounds  
399 in the closed or intermediate configurations, in a manner reminiscent to what it does with  
400 ATP (36,44). First generation type I RET inhibitors like vandetanib (ZD6474) and  
401 nintedanib (BIBF1120) get accommodated parallel to the hinge and perpendicular to the  
402 inner part of the  $\alpha$ C helix (Fig. 3K). On the other hand, second-generation RET inhibitors  
403 accommodate in the path towards the P-loop below and in diagonal from the hinge  
404 across the proximal  $\alpha$ C helix exploiting other druggable hotspots reaching to the solvent  
405 pocket, FP-I and FP-II (Fig. 3L). Taking as a reference the crystal structure of FGFR2  
406 in complex with ATP (PDB 2PVF) (44), we observed the adenine group of ATP forming  
407 hydrogen bonds with E565 and A567 at the hinge mirroring the interactions of RET A807  
408 and Y806 hinge residues with the pyrazolo-pyridine and methyl-pyrazol groups from  
409 LOXO-292 and BLU-667, respectively. Furthermore, hydrogen bonds between FGFR2  
410 main chain N571 and R630 atoms and the ribose of the adenosine moiety were formed.  
411 In the case of RET equivalent residues e.g. L881 made hydrophobic contacts with the  
412 inhibitors and in the case of S811 it was shown to form a water bridge with the  
413 quinazoline group of vandetanib (37). In FGFR2 the catalytic K515 (as part of the post-  
414 lysine pocket) form a salt bridge and hydrogen bonds with  $\alpha$  and  $\beta$  phosphate groups,  
415 whereas in the case of RET the equivalent K758 formed pi-cation interactions with  
416 fluoropyrazole and methoxypyridine rings from BLU-667 and LOXO-292 respectively.



417 FGFR2 F492 (equivalent to RET F735) and A491 (RETG733) main chain atoms formed  
418 hydrogen bonds with the  $\gamma$ -phosphate group of the ATP, and this was mirrored in the  
419 case of LOXO-292 crystal structure by two coordinated water molecules interacting with  
420 main chains G733 and E734 atoms from the P-loop. Altogether, these data demonstrate  
421 that LOXO-292 and BLU-667 target the post-lysine pocket by promoting and open GRL  
422 conformer and exploiting extensive ATP mimicry a feature not observed before with  
423 inhibitors of the first generation.

424

#### 425 **5. Molecular dynamics and stability of apo and complexed structures**

426 The stability and dynamics of RET kinase in the apo (PDB 2IVS) and complexed with  
427 LOXO-292 (PDB ID 7JU6), BLU-667 (PDB ID 7JU5) and ZD6474 (i.e. Vandetanib, PDB  
428 ID 2IVU) were investigated using a 300-ns conventional MD simulation.

429 The root mean-square deviation (RMSD) of the protein  $C\alpha$  atom with respect to the initial  
430 frame was computed to assess the stability of each protein-ligand complex system  
431 compared with the apo state (Fig. 4A). Initial examination of the computed RMSD profile  
432 showed that all the complexed systems equilibrated rapidly with average fluctuations  
433 values of 2 Å, as shown in Fig. 4A. The apo system, on the contrary, displays significant  
434 conformational changes with average RMSD values above 2.5 Å, characterized by  
435 significant conformational changes in the P-loop (Fig. 4A).

436 We also used root-mean square fluctuation (RMSF) calculations to evaluate the effect of  
437 ligand binding on overall protein flexibility during the simulation process. General  
438 inspection of the RMSF profiles revealed a significant reduction in the P-loop flexibility  
439 by LOXO-292 and BLU-667 as a result of the occupation of both FP-II and post-lysine  
440 pocket, resulting in the stabilization of the P-loop in an open conformation. RET-ZD6474  
441 and apo, on the contrary, demonstrated high flexibility in the P-loop, which is consistent  
442 with the structural analysis of the average structure (Fig. 4B). These data together prove  
443 that LOXO-292 and BLU-667 have a direct impact on reducing the flexibility of the P-

444 loop loop by forcing it to an open conformation that is required for post-lysine pocket  
445 occupancy.

446 Next, the MM/GBSA (molecular mechanics Boltzmann surface area) method (35) (32)  
447 was used to estimate each inhibitor binding free energies (Table 1). The calculated  
448 binding free energy ( $G_{total}$ ) of RET-LOXO-292 and -BLU-667 complexed systems were  
449  $-55.1 \pm 4.1$  and  $-49.1 \pm 3.3$  Kcal/mol respectively, which were significantly lower than the  
450 one observed for the RET-ZD6474 complex ( $-43.7 \pm 2.6$  Kcal/mol) indicative of higher  
451 affinity binding by the second-generation RET inhibitors. According to table 1, the van  
452 der Waal interactions are the main drivers for the stability of LOXO-292 and BLU-667,  
453 with energies of  $-66.0 \pm 3.2$  and  $-61.7 \pm 2.7$  Kcal/mol, respectively (vs  $-52.9 \pm 2.3$   
454 Kcal/mol ZD6474). We also noticed that BLU-667 and ZD6474 have similar electrostatic  
455 interactions energies of  $-20.7 \pm 4.4$  and  $-21.0 \pm 3.5$  Kcal/mol, respectively with LOXO-  
456 292 having the lower electrostatic interaction energy of  $-10.7 \pm 4.5$  Kcal/mol. This was  
457 further corroborated by the per-residue energy decomposition analysis that identified the  
458 residues that contributed significantly to the ligand binding through intermolecular  
459 interactions (Fig. 4C). The distinct binding modes of LOXO-292 and BLU-667 that result  
460 in FP-II occupancy allowed the molecules to form strong interactions with P-loop  
461 residues G731, E732, G733, and G736, which stabilized the P-loop into an open-  
462 conformer. Despite access to the post-lysine pocket by LOXO-292 and BLU-667, the  
463 terminal 2-methoxypyridine moiety of LOXO-292 formed stronger interactions with the  
464 side chains of K758, L760, E768, and L772. Furthermore, 2-methoxypyridine formed  
465 significant electrostatic interactions (cation- $\pi$ ) with the side chain of K758, resulting in  
466 an energy value of  $-5.8$  Kcal/mol compared to BLU-667, which only formed a  
467 hydrophobic interaction and had an energy value of  $-3.8$  Kcal/mol. LOXO-292 and BLU-  
468 667 appear to specifically interact with the R878 from the catalytic loop (Fig. 4C). Despite  
469 all the inhibitors formed hydrogen bonds with the hinge, gatekeeper pocket occupation  
470 by ZD6474 resulted in a stronger van der Waal interaction with the side chain of V804,  
471 making ZD6474 susceptible to acquired resistant mutations at that pocket. LOXO-292,

472 BLU-667, and Vandetanib all formed strong interactions with the solvent front region, in  
473 particular residue G810, with total energy values of -2.7, -2.6, and -2.9 Kcal/mol,  
474 respectively. Interestingly, refractory mutations at these sites that reduce the affinity of  
475 these inhibitors and confer resistance have been already identified in patients (41,45)

476

## 477 **6. Functional evaluation of mutants targeting the post-lysine pocket reveals an** 478 **impact on both inhibitor sensitivity and RET tyrosine kinase activity**

479 In order to investigate the impact of post-lysine pocket residues on inhibitor binding and  
480 cellular response, we applied a multidisciplinary approach combining protein  
481 biochemistry, biophysics and cell-based assays. First, we generated recombinant RET  
482 KD WT and post-lysine pocket variants K758M, L760A, L772A and L760/772A (Fig. 5A).  
483 In addition, we also generated a KD V804M mutant as a negative control for the binding  
484 of a prototypical type-I inhibitor e.g. ZD6474. Next, we applied two independent DSF  
485 methods: i) a direct method measuring intrinsic fluorescence upon a fast temperature  
486 gradient providing an inflection temperature ( $T_i$ ), and ii) an indirect method based on  
487 SYPRO™ orange dye that provides melting temperatures ( $T_m$ ). We measured the effect  
488 of LOXO-292 and BLU-667 binding on the thermal stability of the apo-control versus  
489 complexed proteins (Fig. 5B and table 2), ZD-6474 was also tested as a negative control  
490 for the gatekeeper mutant V804M. While both LOXO-292 and BLU-667 binding to RET  
491 KD WT conferred a significant increment in the protein thermal ( $\Delta T_{i/m}$ ) of about 10 °C.  
492 Mutations of some of the post-lysine pocket composites resulted in a significant effect  
493 on the binding of the inhibitors, in particular we observed a detrimental LOXO-292  
494 binding effect to L772A with a lower  $T_m$  of 7.0 °C (vs 9,5 °C control WT), whereas the  
495 double mutant L760/772A had a larger BLU-667  $T_m$  of 14.0 °C (vs 11,6 °C control WT).  
496 Furthermore, the K758M mutant displayed a significant thermal stability increment by  
497 LOXO-292 and BLU-667 of 11,9 and 14,2 °C (vs 9,5 and 11,6 °C control WT,  
498 respectively). The results from the K758M and double L760/772A mutants were

499 surprising to some extent as we anticipated that perturbation of the post-lysine pocket  
500 composites would result in a detrimental effect on the binding on these inhibitors (see  
501 discussion). Next, we tested the effect of post-lysine pocket mutants on the phospho-  
502 tyrosine kinase activity of the RET KD in vitro in time course auto-phosphorylation assays  
503 (Fig. 5C). We found that, contrary to the L760A mutant, which displayed comparable  
504 levels to the WT, RET L772A had a loss of function effect on the tyrosine kinase activity  
505 as indicated by both total phospho-tyrosine and phospho-specific RET Y905 antibodies.  
506 The same detrimental effect was observed with the double L760/772A mutant. Finally,  
507 in order to recapitulate these results in cell-based assays we used HEK293 cells  
508 ectopically expressing a full-length RET receptor with a C634R mutation in the  
509 extracellular domain, which bypasses the GDNF ligand and co-receptor requirements for  
510 activation (with intact intracellular domain) subjected to a dose-dependent treatment with  
511 LOXO-292 and BLU-667 for 90 min (Fig. 5D). While treatment of RET WT KD with  
512 increasing concentrations of LOXO-292 and BLU-667 resulted in a consistent inhibition  
513 of RET auto-phosphorylation and ERK1/2 downstream activity at 10 nM, no significant  
514 differences were observed with the L760A mutant. In the case of the L772A mutant, as  
515 anticipated from the kinase assays we found a loss of function effect. Strikingly the  
516 double L760/772A mutant had a rescue effect on the tyrosine kinase activity by the  
517 L760A mutation, displaying also increased sensitivity to LOXO-292 and BLU-667 as 1  
518 nM concentrations of the inhibitors resulted in a significant reduction on RET auto- and  
519 ERK1/2- phosphorylation levels. As a control we used RET KD V804M, which was  
520 sensitive to both LOXO-292 and BLU-667 at similar concentrations than the WT, but was  
521 resistant to ZD6474 treatment. These data were consistent with the DSF results, and  
522 showed the important implications of the post-lysine pocket composites on both inhibitor  
523 sensitivity and RET tyrosine kinase activity.

524

525

526

527 **DISCUSSION**

528 LOXO-292 and BLU-667 are recently developed second-generation RET inhibitors with  
529 a potent and selective activity against a wide range of RET fusions and mutations in both  
530 preclinical and clinical models (13-15) with a remarkable patient response observed in  
531 phase I and II clinical trials (13-15,17). The main purpose of this study is to explain the  
532 structural and dynamical determinants conferring high selectivity by these RET inhibitors  
533 through a comprehensive computational, structural and functional characterization. We  
534 defined the post-lysine pocket as a key structural determinant for efficient and selective  
535 RET kinase inhibition with important consequences on RET tyrosine kinase activity.

536         Extensive analysis of the active site showed that potent and selective RET kinase  
537 inhibition requires the exploitation of vulnerabilities beyond the occupation of the  
538 adenine- binding pocket and gate-keeper vicinity. We show that the intrinsic flexibility of  
539 the P-loop and the  $\alpha$ C helix reshapes the druggability landscape in the RET active site  
540 (Fig. 1). While in the closed P-loop structure only the adenine-binding, gate-keeper and  
541 solvent pockets were potentially druggable, in the intermediate and open P-loop  
542 structures the FP-II appeared with a significant higher druggability potential relative to  
543 the adenine-binding site. This pocket is distinguished by the existence of a small cryptic  
544 sub-pocket adjacent to the catalytic lysine defined by K758, L760, E768, and L772 that  
545 we defined as the post-lysine pocket. This cryptic pocket was fully accessible in the case  
546 of the open RET structures. The assembly of these residues and the accessibility to the  
547 post-lysine pocket was regulated by the position of F735 side chain, which is directly  
548 coordinated by the dynamics of the P-loop and the positioning of the  $\alpha$ C helix. An  
549 interesting observation is that, as part of the adenine-binding site, the gatekeeper sub-  
550 pocket was found only in the structures with an intermediate and open P-loop  
551 configuration. This is related to the F735 side chain transitioning away from the post-  
552 lysine pocket, which creates more space for the K758 side chain. The recently  
553 discovered S904F mutation in the activation loop of RET resulted in acquired ZD6474  
554 resistance (46). The crystal structure of the RET KD S904F mutant (PDB ID 6FEK)

555 revealed a closed P-loop conformer with an unusual K758 side chain rotamer with NZ  
556 atom pointing towards the gatekeeper pocket. A superimposition of this structure with  
557 the RET KD complexed to ZD6474 (PDB ID 2IVU) revealed steric clashes between the  
558 inhibitor and K758 side chain. This is further supported by a shorter V804-K758 distance  
559 when compared to other closed P-loop structures (table S1). In addition, long-unbiased  
560 MD simulation of RET KD WT and mutant S904F complexed with ZD6474 revealed  
561 higher energy state of the mutant kinase with intermediate P-loop configuration with  
562 F735 pointing towards the active site. As a result, we anticipate that K758 regulates the  
563 accessibility to the gatekeeper pocket as a result of the crosstalk between the gatekeeper  
564 and the post-lysine pockets by the positioning of F735 side chain.

565 RIP MD simulations to show that extensive (RIPlig) and site-directed (L-RIP)  
566 perturbation of the P-loop disrupts the close tether and induces an opening of the P-loop  
567 and active site, consequently expanding the druggability landscape, being F735 the key  
568 determinant for such transition (Fig. 2). Furthermore, we examined the presence and  
569 conservation of the FP-II and post-lysine pocket in other protein kinases that are  
570 pharmacologically inhibited by RET tyrosine kinase inhibitors for which structural  
571 information was available (Fig. 2). We found that conservation of the post-lysine pocket  
572 is also a common feature of the phylogenetically closer group of RTKs (i.e. FGFR1-4,  
573 VEGFR1-2), but is not sufficient for occupancy and competency as dynamic inputs from  
574 the P-loop and  $\alpha$ C restrict access to the pocket. A fully accessible and druggable post-  
575 lysine pocket requires of a synchronous P-loop-open and  $\alpha$ C-in configuration only seen  
576 in RET crystal structures.

577 Superimposition of RET kinase domain crystals structures in complex with LOXO-292  
578 and BLU-667 (21,22,41) with crystal structures of RET in complex with type-I inhibitors  
579 (37,38) showed that both compounds could only fit into the active site in an open P-loop  
580 state (Fig. 4) in the closed or intermediate configurations it would clash with the  
581 compounds, in a reminiscent manner to ATP (36). The free energy calculations by the  
582 MM/GBSA method shows that LOXO-292 and BLU-667 forms important interactions with

583 L730 ( $\beta$ 1) and V738 ( $\beta$ 2), both from the P-loop, and also with hinge residues Y806, K808  
584 and G810. Interestingly, refractory mutations in those sites have been found in patients  
585 and resistant cell lines and clones (Solomon et al., 2020; Subbiah et al., 2020). This is  
586 due to steric clashes with the inhibitors caused by the replacement of bulky amino acid  
587 chains in those regions, as well as the disruption of strong intermolecular hydrophobic  
588 contacts as shown by MM/GBSA analysis (45,47).

589 Functional characterization of mutants targeting the post-lysine pocket revealed  
590 a dual role on drug sensitivity and tyrosine kinase activity. The results from the double  
591 mutant (L760/772) and K758M were surprising as we anticipated that perturbation of the  
592 post-lysine pocket composites would result in a priory detrimental effect on the binding  
593 on these inhibitors. However, a tighter binding was observed in these cases as indicated  
594 by increased  $T_m$  and  $T_i$  (Fig. 5 and table 2). This can be potentially explained by the fact  
595 that substitutions by shorter side chains may allow a better accommodation of the  
596 compounds into the post-lysine pocket, resulting in a sensitizing effect as seen with the  
597 double mutant (L760/772A) (Fig. 5D). In auto-phosphorylation assays using recombinant  
598 isolated RET kinase, the L760A mutant appeared to have higher background  
599 phosphorylation levels which were slightly enhanced over the time course compared with  
600 WT (Fig. 5C). These results suggest the a L760A mutant could be a better substrate for  
601 Sf9 endogenous kinases, as seen before by both oncogenic mutations targeting the  
602 kinase domain (in particular M918T) and mutants disrupting the closed auto-inhibited  
603 tether (36). On the contrary, L772A and L760/772A both had a significant detrimental  
604 effect on RET phospho-tyrosine kinase activity (Fig. 5C). When the same mutants were  
605 evaluated in a RET full-length context in dose-dependent cell-based assays (Fig. 6D) we  
606 obtained results in line with the recombinant protein data e.g. a loss of function effect by  
607 the L772A mutation. Strikingly we also found a rescue effect by the L760A mutation and  
608 increased sensitivity by the double mutant L760/772A. These data were supported by  
609 the binding and DSF data where both L760/772A and the K758M mutants displayed a  
610 significant increment in their  $T_m$  and  $T_i$  upon inhibitor binding (Table 2). These results



611 suggested that mutating specific post-lysine pocket components to alanine favored the  
612 binding potentially by allowing a better accommodation of the 2-methoxypyridine (LOXO-  
613 292) and 4-fluoropyrazole (BLU-667). Furthermore, the striking effect of the double  
614 mutant in terms of rescuing the null effect of the L772A mutation indicates a potential  
615 crosstalk between the  $\beta$ 3- $\alpha$ C loop and the  $\alpha$ C helix, together with L772, which forms part  
616 of a recently described PIF-like pocket in RET (38). In both cases, there are clear signs  
617 of allosteric inputs to the catalytic site by regulating also R- and C-spines assemblies.  
618 We hypothesize that development of next generation RET inhibitors with improved  
619 selectivity and efficacy will require of chemical optimizations that will: i) minimize contacts  
620 and interactions with the solvent pocket and  $\beta$ 3, ii) favor accommodation of the 2-  
621 methoxypyridine (LOXO-292) and 4-fluoropyrazole (BLU-667) groups into the post-  
622 lysine pocket, iii) provide larger space between the gate-keeper residue and the catalytic  
623 lysine to overcome gate-keeper drug resistant mutations and iv) target the catalytic loop  
624 pocket residues, according to our FTsite and MM/GBSA data. Altogether the  
625 identification of the post-lysine pocket as a cryptic druggable vulnerability in the RET  
626 kinase exploited by second generation RET inhibitors has important implications for  
627 future drug design and the development of more potent and specific (allosteric) inhibitors  
628 and personalized therapies for patients with RET-driven cancers.

629

## 630 **FIGURE LEGENDS**

631 **Figure 1. RET active site druggability landscape is determined by the dynamics of**  
632 **the P-loop**

633 (A) Cartoon representation of RET KD crystal structure with two discrete conformations  
634 of the P-loop (PDB 4CKJ). Hydrogen bonds and salt bridge interactions defining both  
635 open (upper) and close (lower) conformations.



636 (B) Superimposition of the indicated RET KD crystal structures depicting side chains of  
637 F735 from the P-loop and catalytic K758 ( $\beta 3$ ) and their corresponding distances ( $\text{\AA}$ ) and  
638 defined volumes of the active site ( $\text{\AA}^3$ ) in each configuration.

639 FT-site mapping of druggable pockets within the active site (color coded) of RET under  
640 different P-loop configurations: (C) Open (PDB 5AMN), (D) intermediate (PDB 2IVT and  
641 2IVV) and (E) closed (PDB 2IVS) depicting residues contributing to each pocket, ABP  
642 (adenine-binding pocket), FP-II (front pocket-II) and catalytic loop-HRD motif pocket  
643 (CP). Surface representation (C-D insets) with side-chain of residues defining a front  
644 subpocket-II defined by K758, L760, L772 and E775. Please note that a fully competent  
645 (available) pocket appears in the open crystal structure, being mutually exclusive with  
646 presence (occupancy) by the side chain of F775.

647

648 **Figure 2. Structural identification and dynamical characterization of a druggable**  
649 **post-lysine pocket**

650 (A) Surface representation of RET post-lysine pocket composites under different P-loop  
651 configurations with amino acid side chains represented in sticks: open (PDB 5AMN),  
652 intermediate (PDB 2 IVT) and closed (PDB 2 IVS). In the case of RET a fully competent  
653 post-lysine pocket is available when the side chain of residue 735 is pointing away from  
654 the active site (open P-loop) and E768 is pointing inwards.

655 (B) Evolutionary conservation of post-lysine pocket composites using ConSurf (48),  
656 closer view of the pocket (inset, dark-red indicates high evolutionary rate)

657 (C) Protein sequence alignment with secondary structural elements of a set of protein  
658 tyrosine kinases which are targets of known RET TKIs for which structural information is  
659 available showing conservation of post-lysine pocket residues (\*).

660 (D) Cartoon representation of a superimposition of crystal structures from (C) with RET  
661 post-lysine pocket residues depicted (RET, VEGFR1, VEGFR2, FGFR1, FGFR2,  
662 FGFR3, FGFR4 and PDGFR $\alpha$ ). (E) Schematic representation of a competent post-lysine

663 pocket: left panel, array of different P-loop configurations (from versus RET  $\alpha$ C-in. Right  
664 panel, array of different  $\alpha$ C helices configurations versus RET open P-loop.

665

666 **Figure 3. LOXO-292 and BLU-667 target the post-lysine**

667 (A) Cartoon representation of RET KD crystal structure in complex with BLU-667 (PDB  
668 7JU5) with colour coded secondary structural elements.

669 (B) Close-up view of the active site in an open (PDB 7JU5) and superimposed closed P-  
670 loop (PDB 2IVS) configuration showing post-lysine pocket residues.

671 (C) 2D-pharmacophore representation of BLU-667 interactions, in color coded:  
672 hydrophobic (yellow), hydrogen bond (red-donor, green-acceptor) and electrostatic  
673 interactions (pi-cation blue).

674 (D) Lateral view of B, without depicting the P-loop.

675 (E) Upper view from B, without depicting the P-loop.

676 (F) Cartoon representation of RET kinase domain crystal structure in complex with  
677 LOXO-292 (PDB 7JU6) with colour coded secondary structural elements.

678 (G) Close-up of the active site in an open and closed P-loop configuration showing post-  
679 lysine pocket residues.

680 (H) 2D-pharmacophore representation of LOXO-292 interactions, in color coded:  
681 hydrophobic (yellow), hydrogen bond (red-donor, green-acceptor) and electrostatic  
682 interactions (pi-cation blue).

683 (I) Lateral view of G, without depicting the P-loop.

684 (J) Upper view from G, without depicting the P-loop.

685 Superimposition of the RET active site (upper view) with gate-keeper and post-lysine  
686 pocket residues, in complex with:

687 (K) ATP based on a crystal structure of FGFR2 (PDB 2PVF), LOXO (PDB 7JU6) and  
688 BLU-667 (PDB 7JU5).

689 (L) ATP (PDB 2PVF), ZD7464 (PDB 2IVU) and BIBF1120 (PDB 6NEC).

690

**691 Figure 5. Molecular dynamics and stability of apo and complexed structures**

692 Computed (A) root mean-square deviation (RMSD), (B) root mean-square fluctuations  
693 (RMSF) of protein backbone C $\alpha$  atoms and (C) per-residue energy decomposition for  
694 RET apo (green), LOXO-292 (black), BLU-667 (red) and ZD6474 complexes throughout  
695 the simulation.

696

**697 Figure 5. Functional evaluation of mutants targeting the post-lysine pocket**

698 (A) Coomassie staining of recombinant RET KD (WT and indicated mutants) samples  
699 across the different purification steps.

700 (B) DSF analyses of apo and complexed proteins WT and indicated mutants by direct IF  
701 (tycho nanotemper, upper panel) and SYPRO orange (lower panel) providing thermal  
702 shifts changes, T<sub>i</sub> and T<sub>m</sub> respectively. For illustrative purposes, a representative  
703 example of RET WT is depicted. See table 2 for full dataset, please note that LOXO-292  
704 samples were not measurable by IF (data not determined, nd).

705 (C) WBs of auto-phosphorylation time courses (0-90 min) with recombinant RET KD WT  
706 and indicated mutants using total phospho-tyrosine and RET phospho-Y905 specific  
707 antibodies. Total protein levels were determined by Coomassie staining.

708 (D) WBs data of lysates from HEK293 cells ectopically expressing RET WT kinase or  
709 the indicated mutants treated with increasing concentrations of the inhibitors LOXO-292  
710 and BLU-667 using the indicated antibodies. ZD6474 was used as an internal control for  
711 the RET KD V804M mutant.

712

**713 Graphic summary**

714 First-generation RET inhibitors were multityrosine kinase inhibitors (TKIs) derived from  
715 secondary pharmacology targeting the adenine-binding pocket that resulted in poor  
716 clinical outputs. Recently developed second-generation RET inhibitors (primary  
717 pharmacology derived) exploit in addition further vulnerabilities within the active site e.g.  
718 the post-lysine pocket. We define the structural and dynamical determinants conferring

719 high selectivity to these inhibitors towards RET by targeting the post-lysine pocket,  
720 making them clinically successful.

721

## 722 **FOOTNOTES**

### 723 **Compliance with ethics requirements**

724 This article does not contain any studies performed with human or animal subjects

### 725 **Declaration of Competing Interest**

726 The authors declare that they have no competing financial interests or personal  
727 relationships that could influence the work reported in this paper.

728

### 729 **Acknowledgements**

730 We thank CNIO Genomics and Proteomics Units and lab members from the Protein  
731 Phosphorylation and Cancer group for their technical assistance. We thank the  
732 Experimental Therapeutic Programme (ETP) and the Spectroscopy and Nuclear  
733 Magnetic Resonance Unit for sharing their expertise and providing helpful comments  
734 and scientific advice. Special thanks to the family of Carmen Gloria Bonnet for their CNIO  
735 Friends contribution.

736

### 737 **Funding**

738 This work was funded by CNIO core funding (BE1115-08), Plan Nacional (BFU2017-  
739 86710-R), Ramón y Cajal (RYC-2016-1938) and Marie Curie WHRI-ACADEMY  
740 International (grant number 608765) grants to IPM and a CNIO-Friends predoctoral  
741 Carmen Gloria Bonnet Fellowship to MAS

742

743 This work was dedicated to Robert M. W. Hofstra (1962-2021), former PhD supervisor  
744 and mentor (IPM)

745

746

747 **REFERENCES**

- 748 1. Blume-Jensen, P., and Hunter, T. (2001) Oncogenic kinase signalling. *Nature*  
749 **411**, 355-365
- 750 2. Zhang, J., Yang, P. L., and Gray, N. S. (2009) Targeting cancer with small  
751 molecule kinase inhibitors. *Nat Rev Cancer* **9**, 28-39
- 752 3. Feng, H. (2019) Tyrosine kinases as druggable targets in cancer
- 753 4. Plaza-Menacho, I. (2018) Structure and function of RET in multiple endocrine  
754 neoplasia type 2. *Endocr Relat Cancer* **25**, T79-T90
- 755 5. Kohno, T., Ichikawa, H., Totoki, Y., Yasuda, K., Hiramoto, M., Nammo, T.,  
756 Sakamoto, H., Tsuta, K., Furuta, K., Shimada, Y., Iwakawa, R., Ogiwara, H.,  
757 Oike, T., Enari, M., Schetter, A. J., Okayama, H., Haugen, A., Skaug, V., Chiku,  
758 S., Yamanaka, I., Arai, Y., Watanabe, S., Sekine, I., Ogawa, S., Harris, C. C.,  
759 Tsuda, H., Yoshida, T., Yokota, J., and Shibata, T. (2012) KIF5B-RET fusions in  
760 lung adenocarcinoma. *Nat Med* **18**, 375-377
- 761 6. Lipson, D., Capelletti, M., Yelensky, R., Otto, G., Parker, A., Jarosz, M., Curran,  
762 J. A., Balasubramanian, S., Bloom, T., Brennan, K. W., Donahue, A., Downing,  
763 S. R., Frampton, G. M., Garcia, L., Juhn, F., Mitchell, K. C., White, E., White, J.,  
764 Zwirko, Z., Peretz, T., Nechushtan, H., Soussan-Gutman, L., Kim, J., Sasaki, H.,  
765 Kim, H. R., Park, S. I., Ercan, D., Sheehan, C. E., Ross, J. S., Cronin, M. T.,  
766 Janne, P. A., and Stephens, P. J. (2012) Identification of new ALK and RET gene  
767 fusions from colorectal and lung cancer biopsies. *Nat Med* **18**, 382-384
- 768 7. Paratala, B. S., Chung, J. H., Williams, C. B., Yilmazel, B., Petrosky, W., Williams,  
769 K., Schrock, A. B., Gay, L. M., Lee, E., Dolfi, S. C., Pham, K., Lin, S., Yao, M.,  
770 Kulkarni, A., DiClemente, F., Liu, C., Rodriguez-Rodriguez, L., Ganesan, S.,  
771 Ross, J. S., Ali, S. M., Leyland-Jones, B., and Hirshfield, K. M. (2018) RET  
772 rearrangements are actionable alterations in breast cancer. *Nat Commun* **9**, 4821
- 773 8. Skalova, A., Vanecek, T., Uro-Coste, E., Bishop, J. A., Weinreb, I., Thompson,  
774 L. D. R., de Sanctis, S., Schiavo-Lena, M., Laco, J., Badoual, C., Santana

- 775 Conceicao, T., Ptakova, N., Baneckova, M., Miesbauerova, M., and Michal, M.  
776 (2018) Molecular Profiling of Salivary Gland Intraductal Carcinoma Revealed a  
777 Subset of Tumors Harboring NCOA4-RET and Novel TRIM27-RET Fusions: A  
778 Report of 17 cases. *Am J Surg Pathol* **42**, 1445-1455
- 779 9. Skalova, A., Ptakova, N., Santana, T., Agaimy, A., Ihrler, S., Uro-Coste, E.,  
780 Thompson, L. D. R., Bishop, J. A., Baneckova, M., Rupp, N. J., Morbini, P., de  
781 Sanctis, S., Schiavo-Lena, M., Vanecek, T., Michal, M., and Leivo, I. (2019)  
782 NCOA4-RET and TRIM27-RET Are Characteristic Gene Fusions in Salivary  
783 Intraductal Carcinoma, Including Invasive and Metastatic Tumors: Is "Intraductal"  
784 Correct? *Am J Surg Pathol* **43**, 1303-1313
- 785 10. Redaelli, S., Plaza-Menacho, I., and Mologni, L. (2018) Novel targeted  
786 therapeutics for MEN2. *Endocr Relat Cancer* **25**, T53-T68
- 787 11. Drilon, A., Hu, Z. I., Lai, G. G. Y., and Tan, D. S. W. (2018) Targeting RET-driven  
788 cancers: lessons from evolving preclinical and clinical landscapes. *Nat Rev Clin*  
789 *Oncol* **15**, 150
- 790 12. Schram, A. M., Chang, M. T., Jonsson, P., and Drilon, A. (2017) Fusions in solid  
791 tumours: diagnostic strategies, targeted therapy, and acquired resistance. *Nat*  
792 *Rev Clin Oncol* **14**, 735-748
- 793 13. Drilon, A., Oxnard, G. R., Tan, D. S. W., Loong, H. H. F., Johnson, M., Gainor,  
794 J., McCoach, C. E., Gautschi, O., Besse, B., Cho, B. C., Peled, N., Weiss, J.,  
795 Kim, Y. J., Ohe, Y., Nishio, M., Park, K., Patel, J., Seto, T., Sakamoto, T., Rosen,  
796 E., Shah, M. H., Barlesi, F., Cassier, P. A., Bazhenova, L., De Braud, F.,  
797 Garralda, E., Velcheti, V., Satouchi, M., Ohashi, K., Pennell, N. A., Reckamp, K.  
798 L., Dy, G. K., Wolf, J., Solomon, B., Falchook, G., Ebata, K., Nguyen, M., Nair,  
799 B., Zhu, E. Y., Yang, L., Huang, X., Olek, E., Rothenberg, S. M., Goto, K., and  
800 Subbiah, V. (2020) Efficacy of Selpercatinib in RET Fusion-Positive Non-Small-  
801 Cell Lung Cancer. *N Engl J Med* **383**, 813-824

- 802 14. Subbiah, V., Gainor, J. F., Rahal, R., Brubaker, J. D., Kim, J. L., Maynard, M.,  
803 Hu, W., Cao, Q., Sheets, M. P., Wilson, D., Wilson, K. J., DiPietro, L., Fleming,  
804 P., Palmer, M., Hu, M. I., Wirth, L., Brose, M. S., Ou, S. I., Taylor, M., Garralda,  
805 E., Miller, S., Wolf, B., Lengauer, C., Guzi, T., and Evans, E. K. (2018) Precision  
806 Targeted Therapy with BLU-667 for RET-Driven Cancers. *Cancer Discov* **8**, 836-  
807 849
- 808 15. Wirth, L. J., Sherman, E., Robinson, B., Solomon, B., Kang, H., Lorch, J.,  
809 Worden, F., Brose, M., Patel, J., Leboulleux, S., Godbert, Y., Barlesi, F., Morris,  
810 J. C., Owonikoko, T. K., Tan, D. S. W., Gautschi, O., Weiss, J., de la  
811 Fouchardiere, C., Burkard, M. E., Laskin, J., Taylor, M. H., Kroiss, M., Medioni,  
812 J., Goldman, J. W., Bauer, T. M., Levy, B., Zhu, V. W., Lakhani, N., Moreno, V.,  
813 Ebata, K., Nguyen, M., Heirich, D., Zhu, E. Y., Huang, X., Yang, L., Kherani, J.,  
814 Rothenberg, S. M., Drilon, A., Subbiah, V., Shah, M. H., and Cabanillas, M. E.  
815 (2020) Efficacy of Selpercatinib in RET-Altered Thyroid Cancers. *N Engl J Med*  
816 **383**, 825-835
- 817 16. Wright, K. M. (2020) FDA Approves Pralsetinib for Treatment of Adults With  
818 Metastatic RET Fusion-Positive NSCLC. *Oncology (Williston Park)* **34**, 406-  
819 406;431
- 820 17. Guo, R., Schreyer, M., Chang, J. C., Rothenberg, S. M., Henry, D., Cotzia, P.,  
821 Kris, M. G., Rekhtman, N., Young, R. J., Hyman, D. M., and Drilon, A. (2019)  
822 Response to Selective RET Inhibition With LOXO-292 in a Patient With RET  
823 Fusion-Positive Lung Cancer With Leptomeningeal Metastases. *JCO Precis*  
824 *Oncol* **3**
- 825 18. Ackermann, C. J., Stock, G., Tay, R., Dawod, M., Gomes, F., and Califano, R.  
826 (2019) Targeted Therapy For RET-Rearranged Non-Small Cell Lung Cancer:  
827 Clinical Development And Future Directions. *Onco Targets Ther* **12**, 7857-7864
- 828 19. Bradford, D., Larkins, E., Mushti, S. L., Rodriguez, L., Skinner, A. M., Helms, W.  
829 S., Price, L. S. L., Fourie Zirkelbach, J., Li, Y., Liu, J., Charlab, R., Reyes Turcu,

- 830 F., Liang, D., Ghosh, S., Roscoe, D., Philip, R., Zack-Taylor, A., Tang, S., Kluetz,  
831 P. G., Beaver, J. A., Pazdur, R., Theoret, M. R., and Singh, H. (2020) FDA  
832 Approval Summary: Selpercatinib for the Treatment of Lung and Thyroid cancers  
833 with RET Gene Mutations or Fusions. *Clin Cancer Res*
- 834 20. Lin, J. J., Liu, S. V., McCoach, C. E., Zhu, V. W., Tan, A. C., Yoda, S., Peterson,  
835 J., Do, A., Prutisto-Chang, K., Dagogo-Jack, I., Sequist, L. V., Wirth, L. J.,  
836 Lennerz, J. K., Hata, A. N., Mino-Kenudson, M., Nardi, V., Ou, S. I., Tan, D. S.,  
837 and Gainor, J. F. (2020) Mechanisms of Resistance to Selective RET Tyrosine  
838 Kinase Inhibitors in RET Fusion-Positive Non-Small Cell Lung Cancer. *Ann Oncol*
- 839 21. Solomon, B. J., Tan, L., Lin, J. J., Wong, S. Q., Hollizeck, S., Ebata, K., Tuch, B.  
840 B., Yoda, S., Gainor, J. F., Sequist, L. V., Oxnard, G. R., Gautschi, O., Drilon, A.,  
841 Subbiah, V., Khoo, C., Zhu, E. Y., Nguyen, M., Henry, D., Condroski, K. R.,  
842 Kolakowski, G. R., Gomez, E., Ballard, J., Metcalf, A. T., Blake, J. F., Dawson,  
843 S. J., Blosser, W., Stancato, L. F., Brandhuber, B. J., Andrews, S., Robinson, B.  
844 G., and Rothenberg, S. M. (2020) RET Solvent Front Mutations Mediate Acquired  
845 Resistance to Selective RET Inhibition in RET-Driven Malignancies. *J Thorac*  
846 *Oncol* **15**, 541-549
- 847 22. Terzyan, S. S., Shen, T., Liu, X., Huang, Q., Teng, P., Zhou, M., Hilberg, F., Cai,  
848 J., Mooers, B. H. M., and Wu, J. (2019) Structural basis of resistance of mutant  
849 RET protein-tyrosine kinase to its inhibitors nintedanib and vandetanib. *J Biol*  
850 *Chem* **294**, 10428-10437
- 851 23. Kozakov, D., Grove, L. E., Hall, D. R., Bohnuud, T., Mottarella, S. E., Luo, L., Xia,  
852 B., Beglov, D., and Vajda, S. (2015) The FTMap family of web servers for  
853 determining and characterizing ligand-binding hot spots of proteins. *Nat Protoc*  
854 **10**, 733-755
- 855 24. Kokh, D. B., Czodrowski, P., Rippmann, F., and Wade, R. C. (2016) Perturbation  
856 Approaches for Exploring Protein Binding Site Flexibility to Predict Transient  
857 Binding Pockets. *J Chem Theory Comput* **12**, 4100-4113



- 858 25. Stank, A., Kokh, D. B., Horn, M., Sizikova, E., Neil, R., Panecka, J., Richter, S.,  
859 and Wade, R. C. (2017) TRAPP webserver: predicting protein binding site  
860 flexibility and detecting transient binding pockets. *Nucleic Acids Res* **45**, W325-  
861 W330
- 862 26. Salomon-Ferrer, R., Gotz, A. W., Poole, D., Le Grand, S., and Walker, R. C.  
863 (2013) Routine Microsecond Molecular Dynamics Simulations with AMBER on  
864 GPUs. 2. Explicit Solvent Particle Mesh Ewald. *J Chem Theory Comput* **9**, 3878-  
865 3888
- 866 27. Maier, J. A., Martinez, C., Kasavajhala, K., Wickstrom, L., Hauser, K. E., and  
867 Simmerling, C. (2015) ff14SB: Improving the Accuracy of Protein Side Chain and  
868 Backbone Parameters from ff99SB. *J Chem Theory Comput* **11**, 3696-3713
- 869 28. Wang, J., Wolf, R. M., Caldwell, J. W., Kollman, P. A., and Case, D. A. (2004)  
870 Development and testing of a general amber force field. *J Comput Chem* **25**,  
871 1157-1174
- 872 29. Darden, T., York, D. and Pedersen, L. (1993) Particle mesh Ewald: An Nlog(N)  
873 method for Ewald sums in large systems. *Journal of Chemical Physics*, **98**,  
874 10089- 10092
- 875 30. Ryckaert, P., Ciccotti, G. and Berendsen, H. J. C. (1977) Numerical integration  
876 of the cartesian equations of motion of a system with constraints: molecular  
877 dynamics of n-alkanes. *Journal of Computational Physics* **23** 327-341
- 878 31. Hunter, J., Henderson, M., and Khan, I. (2007) Collaborative annotation of 3D  
879 crystallographic models. *J Chem Inf Model* **47**, 2475-2484
- 880 32. Wang, E., Sun, H., Wang, J., Wang, Z., Liu, H., Zhang, J. Z. H., and Hou, T.  
881 (2019) End-Point Binding Free Energy Calculation with MM/PBSA and  
882 MM/GBSA: Strategies and Applications in Drug Design. *Chem Rev* **119**, 9478-  
883 9508
- 884 33. Zoete, V., Irving, M. B., and Michielin, O. (2010) MM-GBSA binding free energy  
885 decomposition and T cell receptor engineering. *J Mol Recognit* **23**, 142-152

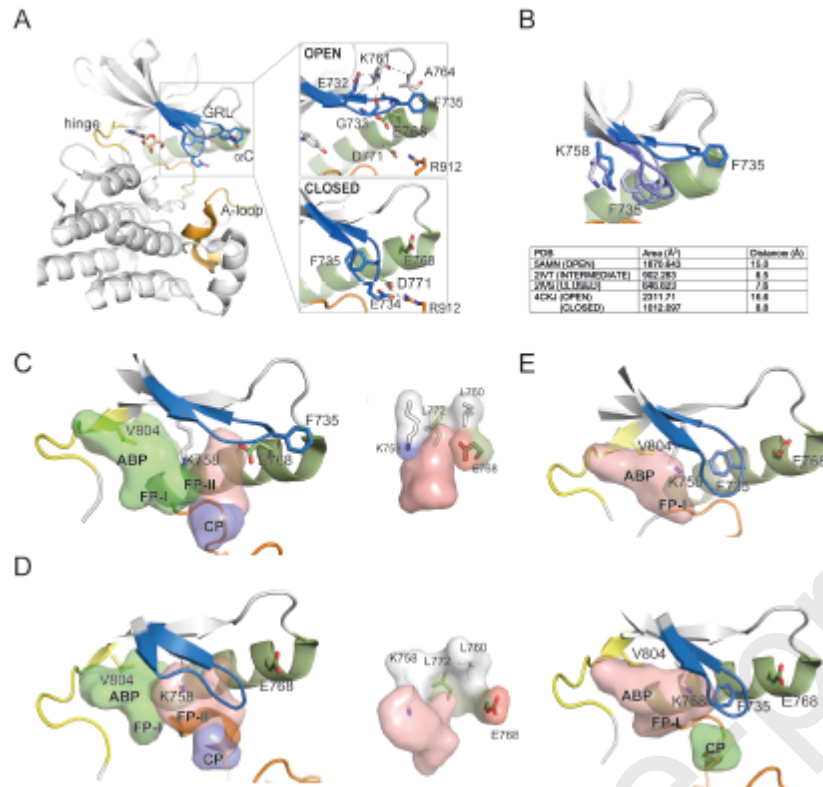
- 886 34. Onufriev, A., Bashford, D., and Case, D. A. (2004) Exploring protein native states  
887 and large-scale conformational changes with a modified generalized born model.  
888 *Proteins* **55**, 383-394
- 889 35. Genheden, S., and Ryde, U. (2015) The MM/PBSA and MM/GBSA methods to  
890 estimate ligand-binding affinities. *Expert Opin Drug Discov* **10**, 449-461
- 891 36. Plaza-Menacho, I., Barnouin, K., Goodman, K., Martinez-Torres, R. J., Borg, A.,  
892 Murray-Rust, J., Moulleron, S., Knowles, P., and McDonald, N. Q. (2014)  
893 Oncogenic RET kinase domain mutations perturb the autophosphorylation  
894 trajectory by enhancing substrate presentation in trans. *Mol Cell* **53**, 738-751
- 895 37. Knowles, P. P., Murray-Rust, J., Kjaer, S., Scott, R. P., Hanrahan, S., Santoro,  
896 M., Ibanez, C. F., and McDonald, N. Q. (2006) Structure and chemical inhibition  
897 of the RET tyrosine kinase domain. *J Biol Chem* **281**, 33577-33587
- 898 38. Plaza-Menacho, I., Barnouin, K., Barry, R., Borg, A., Orme, M., Chauhan, R.,  
899 Moulleron, S., Martinez-Torres, R. J., Meier, P., and McDonald, N. Q. (2016)  
900 RET Functions as a Dual-Specificity Kinase that Requires Allosteric Inputs from  
901 Juxtamembrane Elements. *Cell Rep* **17**, 3319-3332
- 902 39. Plaza-Menacho, I., Morandi, A., Robertson, D., Pancholi, S., Drury, S., Dowsett,  
903 M., Martin, L. A., and Isacke, C. M. (2010) Targeting the receptor tyrosine kinase  
904 RET sensitizes breast cancer cells to tamoxifen treatment and reveals a role for  
905 RET in endocrine resistance. *Oncogene* **29**, 4648-4657
- 906 40. Roskoski, R., Jr., and Sadeghi-Nejad, A. (2018) Role of RET protein-tyrosine  
907 kinase inhibitors in the treatment RET-driven thyroid and lung cancers.  
908 *Pharmacol Res* **128**, 1-17
- 909 41. Subbiah, V., Shen, T., Terzyan, S. S., Liu, X., Hu, X., Patel, K. P., Hu, M.,  
910 Cabanillas, M., Behrang, A., Meric-Bernstam, F., Vo, P. T. T., Mooers, B. H. M.,  
911 and Wu, J. (2021) Structural basis of acquired resistance to selpercatinib and  
912 pralsetinib mediated by non-gatekeeper RET mutations. *Ann Oncol* **32**, 261-268

- 913 42. Plaza-Menacho, I., Mologni, L., Sala, E., Gambacorti-Passerini, C., Magee, A. I.,  
914 Links, T. P., Hofstra, R. M., Barford, D., and Isacke, C. M. (2007) Sorafenib  
915 functions to potently suppress RET tyrosine kinase activity by direct enzymatic  
916 inhibition and promoting RET lysosomal degradation independent of proteasomal  
917 targeting. *J Biol Chem* **282**, 29230-29240
- 918 43. Garner, A. P., Gozgit, J. M., Anjum, R., Vodala, S., Schrock, A., Zhou, T.,  
919 Serrano, C., Eilers, G., Zhu, M., Ketzer, J., Wardwell, S., Ning, Y., Song, Y.,  
920 Kohlmann, A., Wang, F., Clackson, T., Heinrich, M. C., Fletcher, J. A., Bauer, S.,  
921 and Rivera, V. M. (2014) Ponatinib inhibits polyclonal drug-resistant KIT  
922 oncoproteins and shows therapeutic potential in heavily pretreated  
923 gastrointestinal stromal tumor (GIST) patients. *Clin Cancer Res* **20**, 5745-5755
- 924 44. Chen, H., Ma, J., Li, W., Eliseenkova, A. V., Xu, C., Neubert, T. A., Miller, W. T.,  
925 and Mohammadi, M. (2007) A molecular brake in the kinase hinge region  
926 regulates the activity of receptor tyrosine kinases. *Mol Cell* **27**, 717-730
- 927 45. Shen, T., Hu, X., Liu, X., Subbiah, V., Mooers, B. H. M., and Wu, J. (2021) The  
928 L730V/I RET roof mutations display different activities toward pralsetinib and  
929 selpercatinib. *NPJ Precis Oncol* **5**, 48
- 930 46. Nakaoku, T., Kohno, T., Araki, M., Niho, S., Chauhan, R., Knowles, P. P.,  
931 Tsuchihara, K., Matsumoto, S., Shimada, Y., Mimaki, S., Ishii, G., Ichikawa, H.,  
932 Nagatoishi, S., Tsumoto, K., Okuno, Y., Yoh, K., McDonald, N. Q., and Goto, K.  
933 (2018) A secondary RET mutation in the activation loop conferring resistance to  
934 vandetanib. *Nat Commun* **9**, 625
- 935 47. Subbiah, V., Shen, T., Tetzlaff, M., Weissferdt, A., Byers, L. A., Cascone, T.,  
936 Behrang, A., Meric-Bernstam, F., Mooers, B. H. M., Rothenberg, S. M., Ebata,  
937 K., and Wu, J. (2021) Patient-driven discovery and post-clinical validation of  
938 NTRK3 fusion as an acquired resistance mechanism to selpercatinib in RET  
939 fusion-positive lung cancer. *Ann Oncol* **32**, 817-819

- 940 48. Ashkenazy, H., Abadi, S., Martz, E., Chay, O., Mayrose, I., Pupko, T., and Ben-  
941 Tal, N. (2016) ConSurf 2016: an improved methodology to estimate and visualize  
942 evolutionary conservation in macromolecules. *Nucleic Acids Res* **44**, W344-350  
943  
944  
945  
946

Journal Pre-proofs

Figure 1



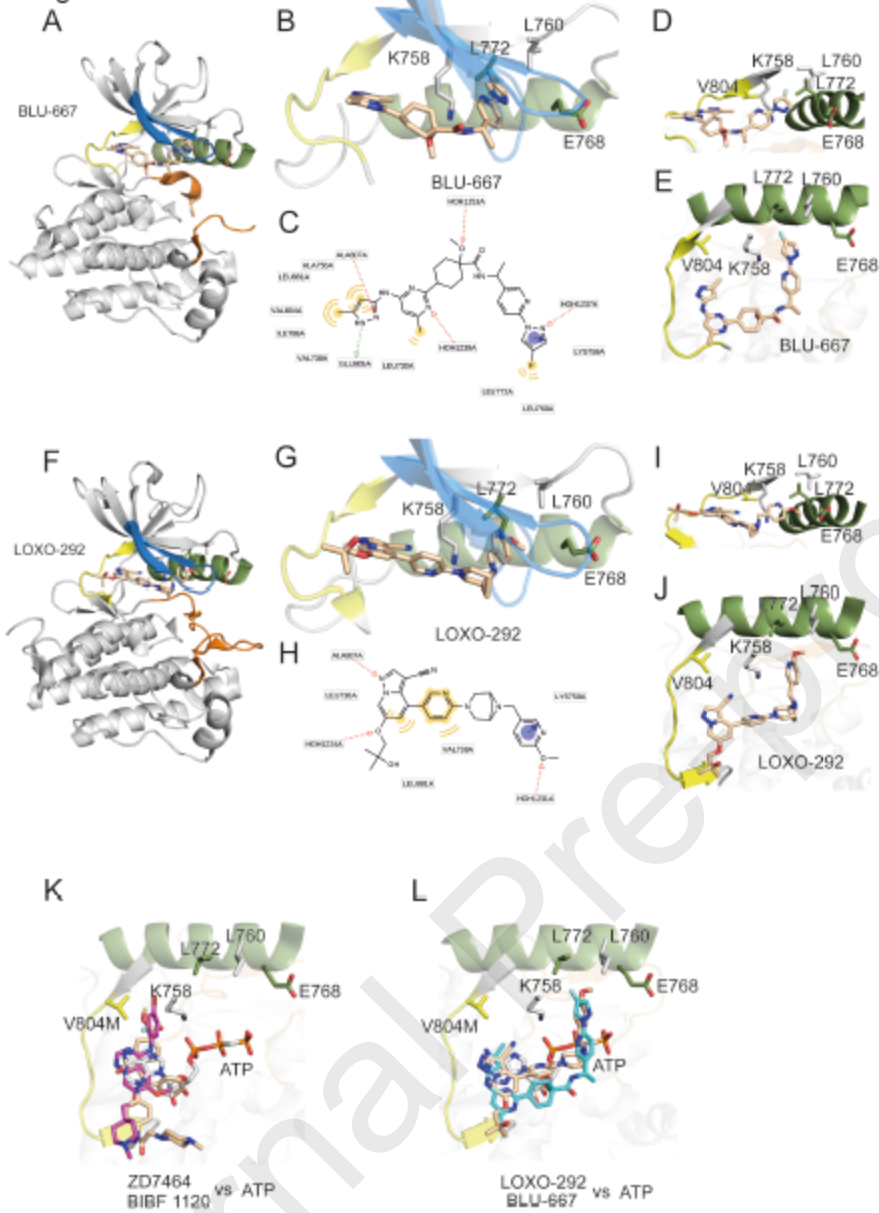
947

948

949



Figure 3



952

953

Figure 4

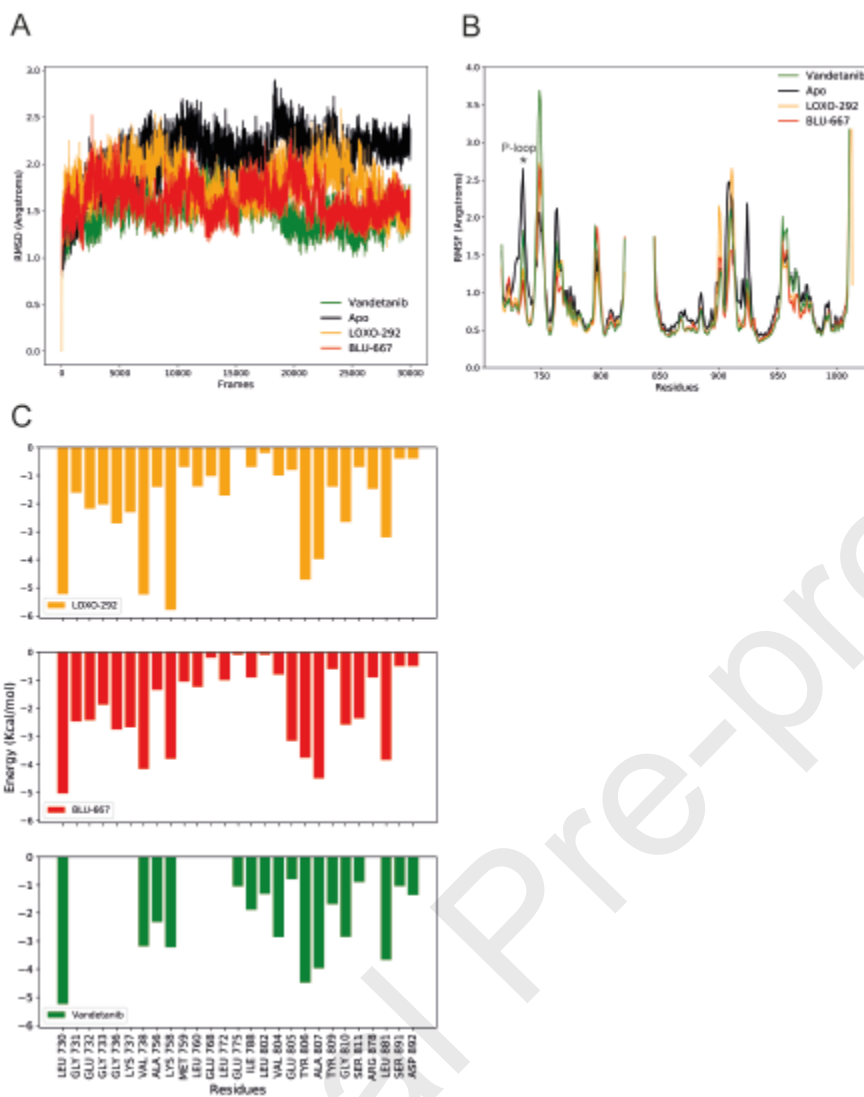
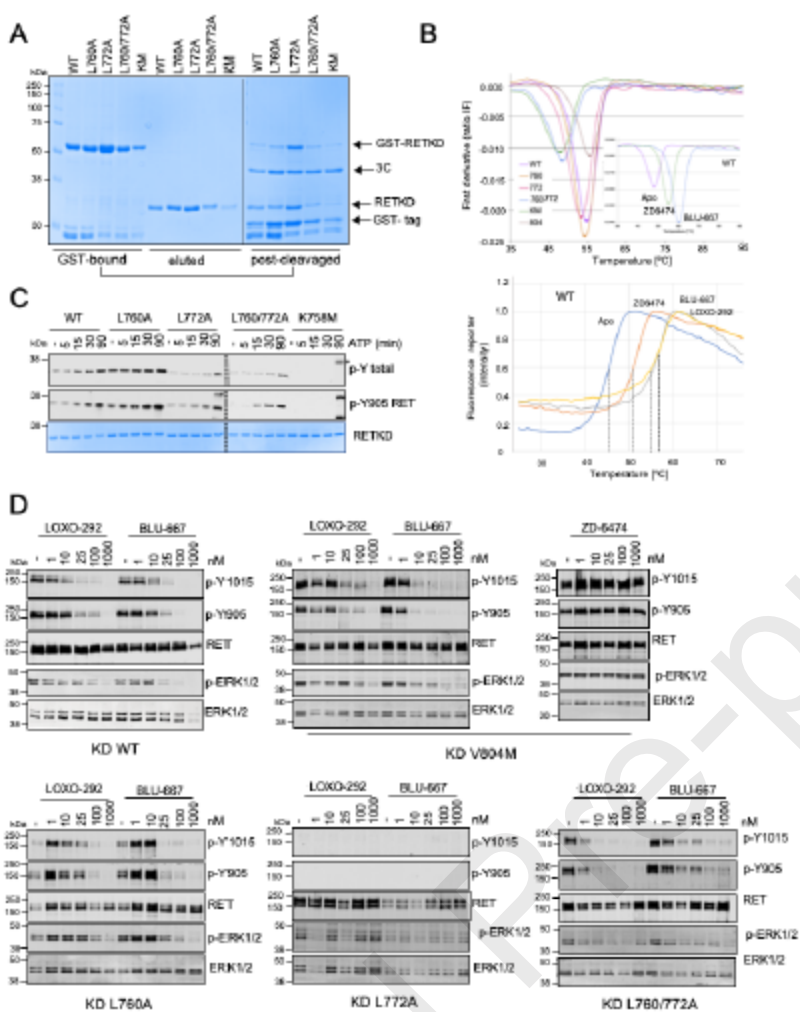




Figure 5



956

957

958 Table 1.

Inhibitor	$\Delta E_{vdw}$	$\Delta E_{ele}$	$\Delta G_{GB}$	$\Delta E_{surf}$	$\Delta E_{gas}$	$\Delta G_{solv}$	$\Delta G_{total}$
LOXO-292	- 66.0 $\pm$ 3.2	- 10.7 $\pm$ 4.5	28.9 $\pm$ 4.1	- 7.4 $\pm$ 0.3	- 76.6 $\pm$ 6.2	21.5 $\pm$ 4.0	- 55.1 $\pm$ 4.1
BLU-667	- 61.7 $\pm$ 2.7	- 20.7 $\pm$ 4.4	40 $\pm$ 3.4	- 6.9 $\pm$ 0.3	- 82.4 $\pm$ 5.2	33.3 $\pm$ 3.3	- 49.1 $\pm$ 3.3
ZD6474	- 52.9 $\pm$ 2.3	- 21.0 $\pm$ 3.5	36.5 $\pm$ 3.3	- 6.2 $\pm$ 0.2	- 73.9 $\pm$ 4.4	30.2 $\pm$ 3.2	- 43.7 $\pm$ 2.6

959

960 Table 2.

		$T_m$ (C°)	deltaTm		$T_i$ (C°)	deltaTi
WT	Apo	44.7 $\pm$ 0.7			55.9 $\pm$ 0.6	
	LOXO292	54.3 $\pm$ 1.7	9.5		n/d	
	BLU667	56.4 $\pm$ 0.5	11.6		66.9 $\pm$ 2.3	10.8
	ZD6447	51.1 $\pm$ 0.6	6.3		60.1 $\pm$ 1.5	4.7
L760A	Apo	42.9 $\pm$ 3.3			54.8 $\pm$ 1.1	
	LOXO292	51.6 $\pm$ 3.3	8.7		n/d	
	BLU667	54.8 $\pm$ 0.4	11.9		66.0 $\pm$ 1.0	11.2
	ZD6447	51.2 $\pm$ 0.6	8.3		60.1 $\pm$ 1.5	5.3
L772A	Apo	41.3 $\pm$ 1.5			53.0 $\pm$ 0.4	
	LOXO292	48.4 $\pm$ 3.8	7.1		n/d	
	BLU667	52.9 $\pm$ 1.1	11.7		65.0 $\pm$ 1.2	12.0
	ZD6447	49.1 $\pm$ 1.2	7.9		58.6 $\pm$ 2.2	5.6
L760/772A	Apo	36.4 $\pm$ 0.5			48.8 $\pm$ 0.3	
	LOXO292	46.8 $\pm$ 1.7	10.9		n/d	
	BLU667	50.5 $\pm$ 0.9	14.09		62.9 $\pm$ 0.7	14.0
	ZD6447	45.8 $\pm$ 0.6	9.3		56.9 $\pm$ 0.7	8.05
K758M	Apo	36.2 $\pm$ 0.2			49.9 $\pm$ 0.7	
	LOXO292	48.2 $\pm$ 2.9	11.9		n/d	
	BLU667	50.5 $\pm$ 0.1	14.2		61.8 $\pm$ 0.6	11.9
	ZD6447	45.2 $\pm$ 0.5	8.9		54.8 $\pm$ 1.3	4.8
V804M	Apo	47.2 $\pm$ 1.3			55.9 $\pm$ 0.4	
	LOXO292	53.6 $\pm$ 1.6	6.4		n/d	
	BLU667	55.8 $\pm$ 1.2	8.7		67.1 $\pm$ 1.6	11.1
	ZD6447	47.0 $\pm$ 1.7	-0.1		55.4 $\pm$ 1.4	-0.5

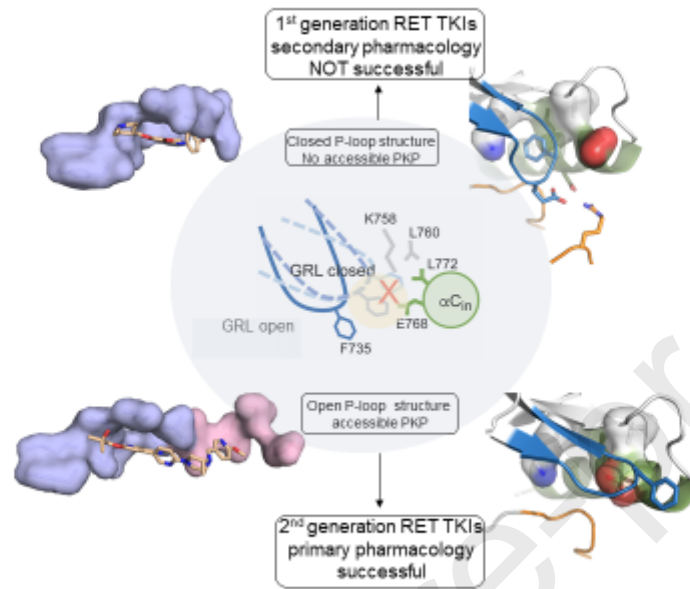
961

962

963

964

965 Graphical abstract



966

967

968

969 **Research highlights Shehata et al.**

- 970 . The druggability landscape of the RET active site is determined by the structural  
971 dynamics of the P-loop and the  $\alpha$ C helix
- 972 . RET selectivity is achieved by the occupancy of a small cryptic pocket adjacent to  
973 catalytic lysine defined by K758, L760, E768 and L772: the post-lysine pocket
- 974 . Efficient occupancy of the post-lysine pocket is restricted to a synchronous P-loop  
975 open  
976 and  $\alpha$ C-in configuration, a distinctive feature of RET crystal structures
- 977 . LOXO-292 and BLU-667 target the post-lysine pocket and exploit extensive  
978 ATP mimicry
- 979 . Engineered mutants targeting the post-lysine pocket impact on inhibitor binding and  
980 sensitivity, as well as RET tyrosine kinase activity